Biosensors and Bioelectronics 189 (2021) 113385

Contents lists available at ScienceDirect

Biosensors and Bioelectronics

journal homepage: www.elsevier.com/locate/bios

One dimensional magneto-optical nanocomplex from silver nanoclusters and magnetite nanorods containing ordered mesocages for sensitive detection of PD-L1

Xing Huang [a,1], Zhao-huan Zhang [b,1], Jie Chen [a,c], Zhihui Mao [a,d], Han Zhu [a], Yawen Liu [c,d], Zhongzheng Zhu [e,*], Hongxia Chen [a,**]

[a] Center for Molecular Recognition and Biosensing, School of Life Sciences, Shanghai University, Shanghai, 200444, PR China
[b] Department of Laboratory Medicine, Changzheng Hospital, Naval Medical University, Shanghai, 200003, PR China
[c] School of Medicine, Shanghai University, Shanghai, 200444, PR China
[d] School of Environmental and Chemical Engineering, Shanghai University, Shanghai, 200444, PR China
[e] Department of Oncology, Shanghai Tenth People's Hospital, Tongji University School of Medicine, 301 Middle Yanchang Road, Shanghai, 200072, PR China

ARTICLE INFO

Keywords:
Surface plasmon resonance
Magnetite nanorods containing ordered mesocages
Silver nanoclusters
PD-L1
Dual selective recognition

ABSTRACT

Programmed death ligand 1 (PD-L1) is a typical immune checkpoint protein, whose up-regulation on the membrane of different tumor cells inhibits the immune response of T cells and leads to the escape of tumor cells. In this work, we designed a facile and highly specific surface plasmon resonance (SPR) biosensor to detect PD-L1 in human plasma based on magnetite nanorods containing ordered mesocages (MNOM) and silver nanoclusters (AgNCs). Magneto-optical nanocomplex MNOM@AgNCs with superior magneto-optical properties and high signal-to-noise ratio were fabricated to improve the detection sensitivity owing to the high specific surface area of MNOM and excellent localized SPR of AgNCs. The PD-L1 Antibody on the surface of gold chip and the PD-L1 aptamer on MNOM@AgNCs could realize dual selective recognition of PD-L1, providing the specificity of the sensor and reducing non-specific binding. The SPR sensor showed a good linear range of PD-L1 from 10 ng/mL to 300 ng/mL with the detection limit of 3.29 ng/mL. The practical performance of this immunosensing platform had been successfully verified by clinical samples which included healthy donors and cancer patients. Based on the analysis, the developed immunosensor provided a new strategy for point-of-care detection of PD-L1 and could be used as clinical companion diagnosis of PD-1/PD-L1 inhibitor therapy.

1. Introduction

Programmed death ligand 1 (PD-L1), the ligand of programmed death protein 1 (PD-1), is widely overexpressed in various cancer cell membranes (Saito et al., 2017; Yu et al., 2016). Recognition between PD-L1 and PD-1 inhibits the activity of T cells, which achieve immune escape and further growth of tumor cells (Jiang et al., 2019; Kim and Chen, 2016). Therefore, PD-L1 has the potential to be a novel biomarker for tumor diagnosis. Immunohistochemistry is the commonly used clinical method for detecting PD-L1 due to its high specificity and accurate positioning (O'Malley et al., 2019; Sound et al., 2018). However, complicated operation steps, high cost, and subjective results also hinder its application (Pang et al., 2020). Hence, it is imperative to develop a facile and cost-effective method for quantitative detection of PD-L1, so as to provide diverse patients with precise treatment and personalized prognosis assessment.

Various types of detection techniques have been widely utilized in the detection of cancer biomarkers, such as colorimetry (Jiang et al., 2017; Ye et al., 2017), electrochemistry (Hasanzadeh et al., 2017; Singh et al., 2019), surface enhanced raman spectroscopy (Cialla-May et al., 2017; Qiao et al., 2018), and surface plasmon resonance (SPR) (Ferhan et al., 2018; Jayanthi et al., 2017). Among these methods, SPR appears to own a lot of outstanding characteristics, for example, high sensitivity, great selectivity, label-free and real-time detection (Zhao et al., 2019;

* Corresponding author.
** Corresponding author.
E-mail addresses: zhuzzmd@tongji.edu.cn (Z. Zhu), hxchen@shu.edu.cn (H. Chen).
[1] Same contributions.

https://doi.org/10.1016/j.bios.2021.113385
Received 12 March 2021; Received in revised form 26 April 2021; Accepted 28 May 2021
Available online 31 May 2021
0956-5663/© 2021 Elsevier B.V. All rights reserved.

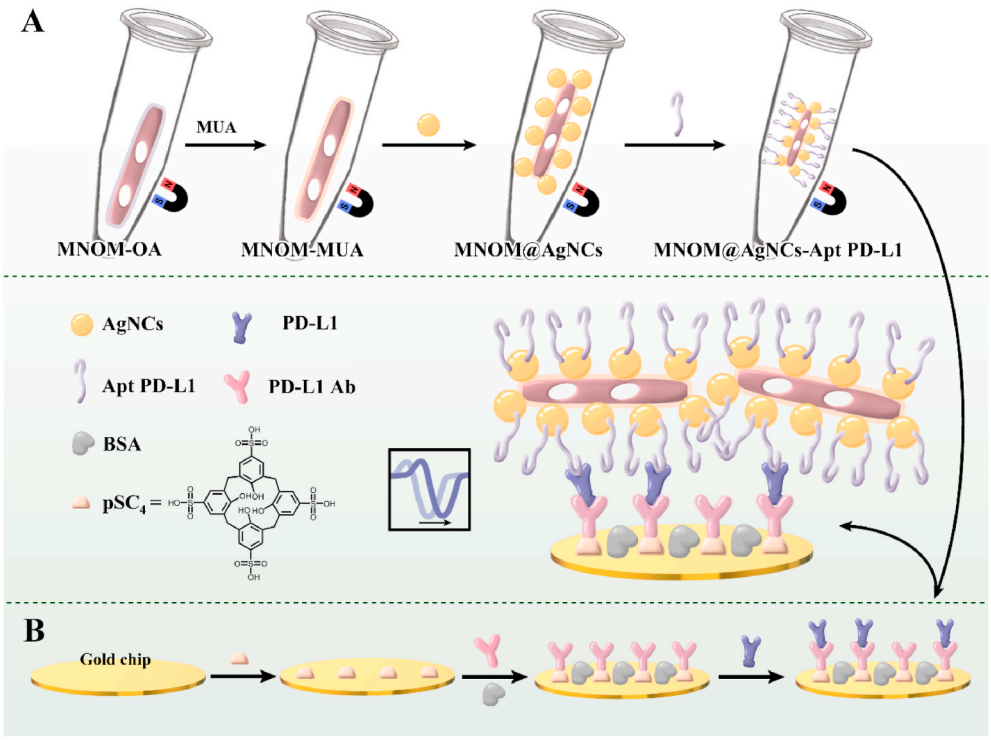

Scheme 1. Schematic diagram of MNOM@AgNCs-Apt PD-L1 magneto-optical nanocomplex with enhanced sensitivity to detect PD-L1.

Zhu et al., 2020).

Magneto-optical (MO) materials are composed of precious metal (e.g., Au, Ag, Pt) and magnetic nanomaterials, and show excellent synergistic characteristics of plasmonic and magnetic properties (Lee and Lee, 2017; Lv et al., 2018; Wu et al., 2016; Zhang et al., 2015). Magneto-optical materials mainly included spherical core-shell or core-satellite materials, heterodimer, multicomponent hybrid materials, and non-spherical core-shell architectures (Zhou et al., 2014). According to the previous study, the signal-to-noise ratio of sensors constructed with MO materials is significantly higher than that of sensors based solely on magnetic nanomaterials (Lee and Lee, 2017).

Lately, it has been reported that one-dimensional magnetite nanorods containing ordered mesocages (MNOM) with template-free and uniform pore size can be used as magnetic component of MO materials because of their higher surface-to-volume ratio, better adsorption capacity and excellent electrical conductivity (Adhikari et al., 2020; Tufa et al., 2020; Wu et al., 2019). This template-free method makes the synthesis process much easier without fabricating and removing the template (Deng et al., 2013; Zhu et al., 2014). One-dimensional MNOM shows anisotropic magnetization characteristics compared with other spherical magnetic materials (Wu et al., 2019). The size of ordered and quasispherical pores can be controlled, so as to more efficiently load small-sized substances, for instance, anti-cancer drugs or noble metal nanoclusters. Silver nanomaterials have better sensitivity than gold owing to their larger real part of dielectric constant (Saleh et al., 2016). Thus, MNOM functionalized with thiol groups could bind with silver nanoclusters (AgNCs) to fabricate multicomponent hybrid magneto-optical materials MNOM@AgNCs (Naaz et al., 2018), which is similar to silver nanorods (AgNRs) with magnetic properties. Compared with bare AgNCs, there are two typical localized surface plasmon resonance (LSPR) peaks of AgNRs: the transverse and the longitudinal. When adjacent AgNRs are close to one another, the electric field at the hotspots in the gap would be greatly enhanced owing to the coupling of LSPRs to each other (Reguera et al., 2017). The strong field at the hotspots and more surface plasmon bands make AgNRs more sensitive to the refractive index (RI) changes in the surrounding solution (Murphy et al., 2008; Zhang et al., 2014). However, although MNOM and AgNCs have the merits of composing a brilliant MO material, there is no relevant research so far.

In this work, a sensitive and facile SPR sensor based on MNOM@AgNCs magneto-optical nanocomplex is developed to achieve quantitative detection of PD-L1 as shown in Scheme 1. MNOM@AgNCs is synthesized by modifying AgNCs onto MNOM through Ag–S bond by one-pot method. Through host-guest recognition and hydrophobic interaction, Anti-PD-L1 (PD-L1 Ab) could bind with pSC4 which is anchored on the gold chip. PD-L1 specific aptamer (Apt PD-L1) is connected to the AgNCs on the magneto-optical nanocomplex. Dual recognition of PD-L1 Ab and Apt PD-L1 with PD-L1 constitutes a typical sandwich structure, enabling selective and quantitative detection of PD-L1. MNOM@AgNCs shows excellent LSPR and strong magneto-optical effect. The results show that the constructed sensor has good feasibility for the determination of PD-L1 and has high sensitivity and low detection limit. Real samples which are collected from healthy donors and cancer patients are utilized to verify the practical performance of the sensor, which demonstrates that the sensing platform can be applied to the clinical detection of biomarkers.

2. Experimental section

2.1. Materials and chemicals

Sodium citrate tribasic dehydrate, Tris(2-carboxyethyl) phosphine hydrochloride (TCEP), 11-Mercaptoundecanoic acid (MUA), Silver nitrate (AgNO3), Ferric chloride (FeCl3), Sodium borohydride (NaBH4), polyethyleneimine, oleylamine, and Sodium hydroxide (NaOH) were purchased from Sigma-Aldrich (Shanghai, China). Disodium hydrogen phosphate (Na2HPO4), Hydrogen peroxide (H2O2), Absolute ethanol (at least purity of 99.7% v/v), Cyclohexanone, Acetone and Bovine serum albumin (BSA) were purchased from Sinopharm Chemical Reagent (Shanghai, China). *para*-Sulfonatocalix[4]arene (pSC4) was received from TCI Development (Shanghai, China). PD-L1 Ab was purchased from ABclonal (ABclonal, China, A1645). PD-L1 was purchased

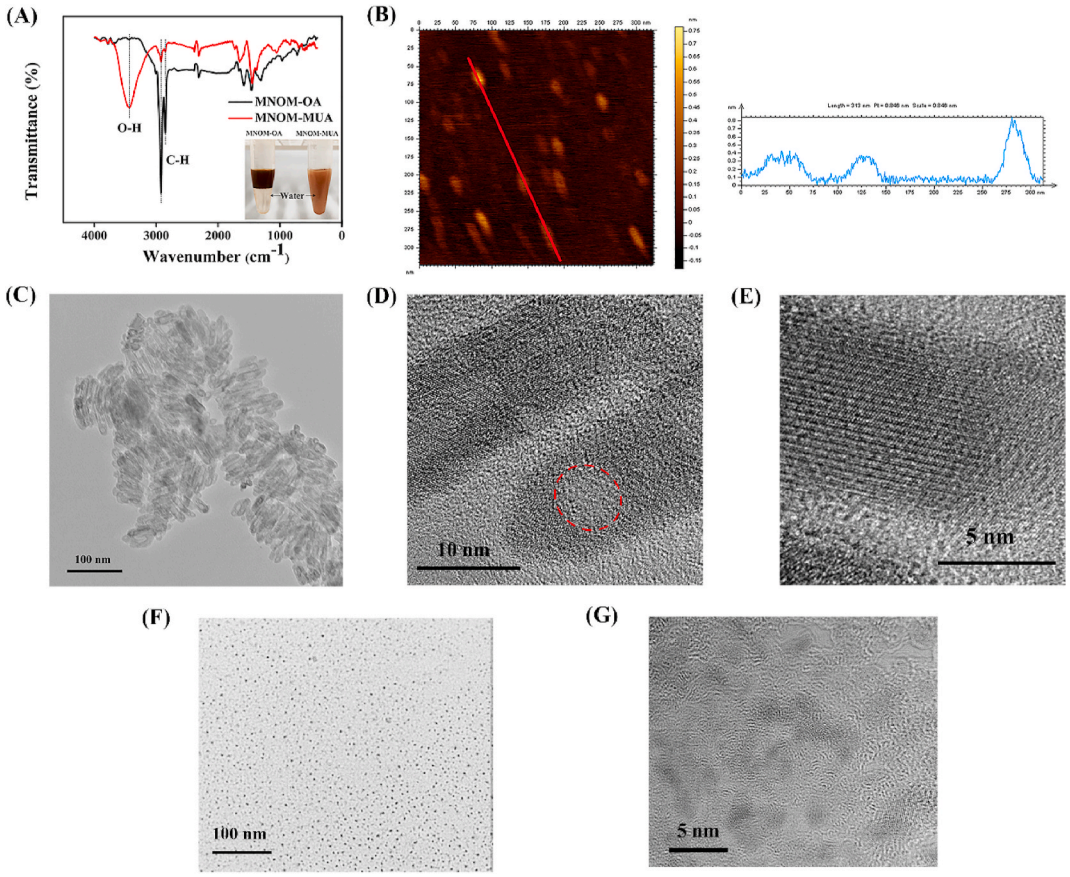

Fig. 1. Characterizations of MNOM and AgNCs: (A) FT-IR spectra of MNOM-OA and MNOM-MUA. Inset: Demonstration of oleylamine -soluble MNOM-OA vs water-soluble MNOM-MUA. (B) 2D AFM images (Left) and line profiles (Right) of MNOM-MUA. TEM image (C) and HRTEM image of the mesocages (D) and MNOM-MUA (E). TEM image (F) and HRTEM image (G) of AgNCs.

from Abcam (Abcam, China, ab130039). PD-L1 Aptamer was synthesized by Sangon Biotech (Shanghai, China) and sequence was 5′- ACG GGC CAC ATC AAC TCA TTG ATA GAC AAT GCG TCC ACT GCC CGT-3′. All chemical reagents used in this work were analytical grade and without further purifications. All the solutions were prepared by deionized water by the Milli-Q distillation system (Branstead, USA).

2.2. Apparatuses

SPR measurements were performed by MP-SPR Navi 210A VASA instrument (BioNavis Ltd, Tampere, Finland). Transmission electron microscope (TEM) images and energy dispersive spectroscopy (EDS) were carried out with JEM-2010F microscope (Japan). Electrochemical characterizations were recorded by Autolab PGSTAT128N system (Eco Chemise B.V., The Netherlands). Scanning electron microscope (SEM) images were recorded by NOVA NanoSEM 450 (FEI, USA). UV–vis spectra were obtained by Shimadzu UV-2450 PC UV–Vis spectrophotometer. Fourier transform infrared (FT-IR) spectra were performed by Bruker 70, Germany. Zeta potential was recorded by Malvern Nano Zetasizer (MAL1202556). Tapping-Mode Atomic Force Microscope (AFM) images were acquired by Agilent AFM-5500 microscope.

2.3. Preparation of AgNCs

AgNCs were synthesized by classical NaBH4 reduction of $AgNO_3$ (Song et al., 2018). First, 100 mL of 0.25 mM $AgNO_3$ solution and 100 mL of 0.25 mM trisodium citrate solution were added and stirred at room temperature for 30 min in a round-bottom flask. 6 mL of 5 mM NaBH4 was added and reacted for 12 h in the dark to obtain AgNCs. The final solution was placed and stored in a 4 °C refrigerator for further use. The glassware used in the experiments was all soaked in aqua regia (HCl: HNO_3 = 3:1, v/v) for 30 min, and rinsed with deionized water.

2.4. Fabrication of MNOM

Typically, one-dimensional magnetite nanorods containing ordered mesocages was prepared according to previous research (Wu et al., 2019). 10 mM $FeCl_3$ and 0.125 mM polyethyleneimine were added into 60 mL deionized water, and heated at 90 °C for 4 h. After centrifuge, the precipitate was washed with deionized water and acetaldehyde for several times and dried at 25 °C. The dried product was added to 10 mL of oleylamine and heated at 200 °C for 4 h to obtain MNOM. TEM and SEM images were performed to characterize MNOM.

2.5. Ligand exchange

The procedure of ligand exchange of MNOM with MUA was similar to the previous study but with some modifications (Bagaria et al., 2006). Firstly, 5 mL of cyclohexanone was added into 25 mg of MUA. 1 mL of MNOM solution was added into uniformly dispersed MUA solution. In order to remove excess oleylamine and MUA, several times of centrifugation at 3500 rpm for 5 min were performed, and the precipitate was re-dissolved in cyclohexanone, ethanol, and acetone, respectively. After the fourth time of centrifugation, the precipitate was re-dissolved in deionized water to obtain the final MNOM solution after ligand exchange, and FT-IR was used to characterize the ligand exchange.

2.6. MNOM@AgNCs-Apt PD-L1 complex (MAAs)

As for AgNCs coupling, freshly prepared AgNCs was added into

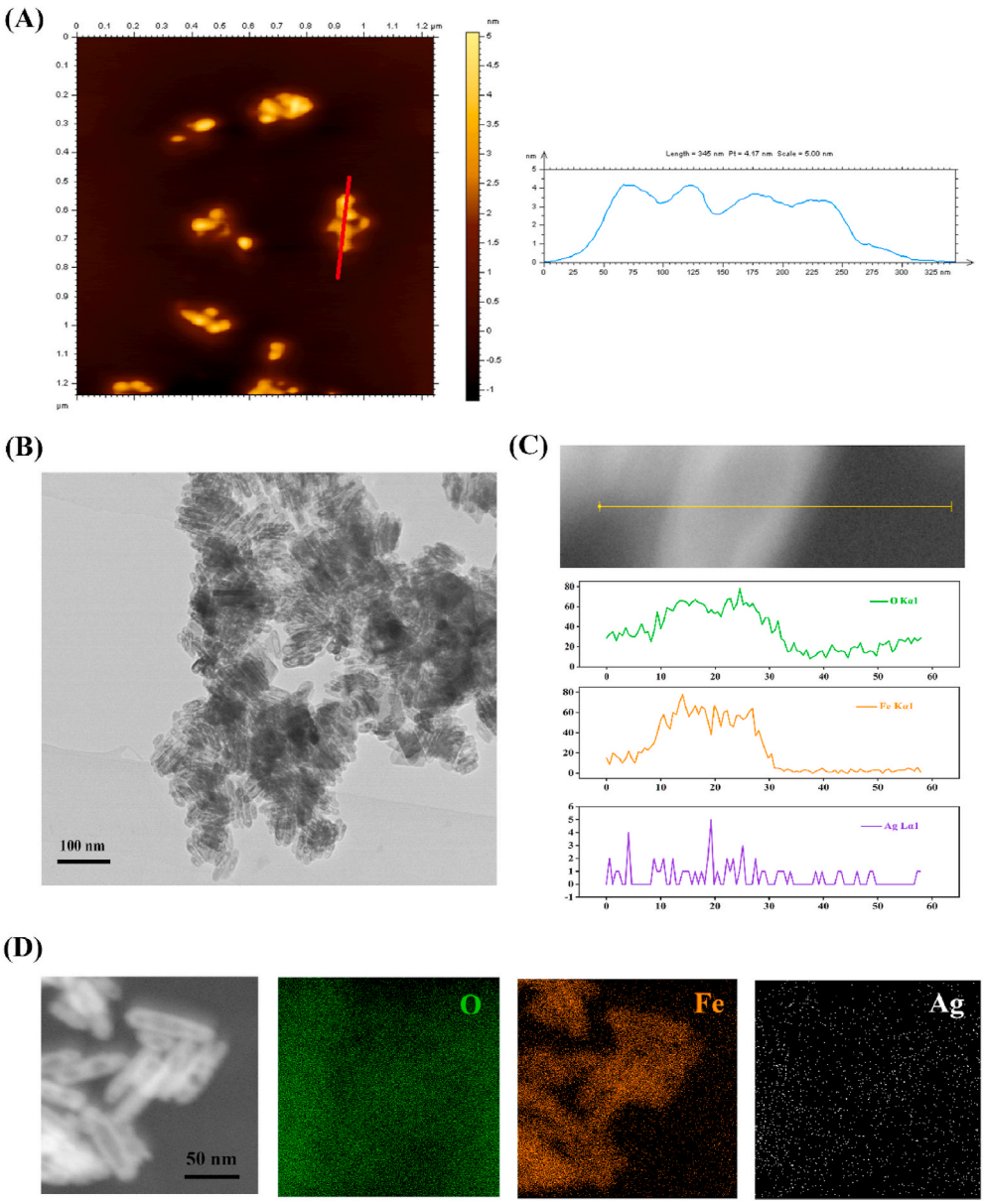

Fig. 2. Characterizations of MNOM@AgNCs: (A) 2D AFM images (Left) and line profiles (Right) of MNOM@AgNCs. TEM image (B) of MNOM@AgNCs. (C) TEM image and corresponding line EDS. (D) Electron microscopy image and EDS element mapping images of O, Fe and Ag in the selected area.

MNOM aqueous solution, and reacted in a 4 °C refrigerator overnight to obtain MNOM@AgNCs. 80 μL of 5 mM TCEP and 20 μL of 10 μM PD-L1 aptamer were mixed well and reacted at room temperature for 40 min, and then added into 100 μL MNOM@AgNCs for 1 h at room temperature to obtain MAAs.

2.7. Electrochemical measurements

The gold electrodes were firstly polished with 0.1 μm and 0.03 μm polishing powder and sonicated in deionized water and ethanol for 3 min. Then the electrodes were soaked with freshly prepared piranha solution (H_2SO_4: 30% H_2O_2 = 3:1) for 5 min. The surface of the electrodes were rinsed with deionized water and dried with nitrogen.

Electrochemical impedance spectroscopy (EIS) and cyclic voltammetry (CV) measurements were utilized to characterize step-by-step modification on the gold electrode. The electrolyte solution was 5 mM $[Fe(CN)_6]^{3-/4-}$ containing 0.1 M KCl. The frequency range of EIS was from 0.1 Hz to 100 kHz. The scanning potential of CV was from 0.8 to -0.8V, while the rate was 100 mV/s.

2.8. Chip functionalization and SPR detections

First, 100 μL of 10 mM pSC_4 was added to the surface of gold chip, and modified for 12 h. Unbound pSC_4 was washed with deionized water slowly and gently. 1.17 μg/mL PD-L1 Ab was added onto the chip surface. After incubation for 40 min, 0.1 mg/mL BSA was added to prevent non-specific adsorption. 200 ng/mL PD-L1 could be anchored on the chip by specific binding of PD-L1 Ab. MAAs could be used to further amplify the SPR signal due to the binding of PD-L1 and Apt PD-L1.

3. Results and disscussion

3.1. Characterization of nanomaterials

As-synthesized MNOM are dispersed in oleylamine (OA) as both stabilizer and reducing agent to prevent the aggregation. However,

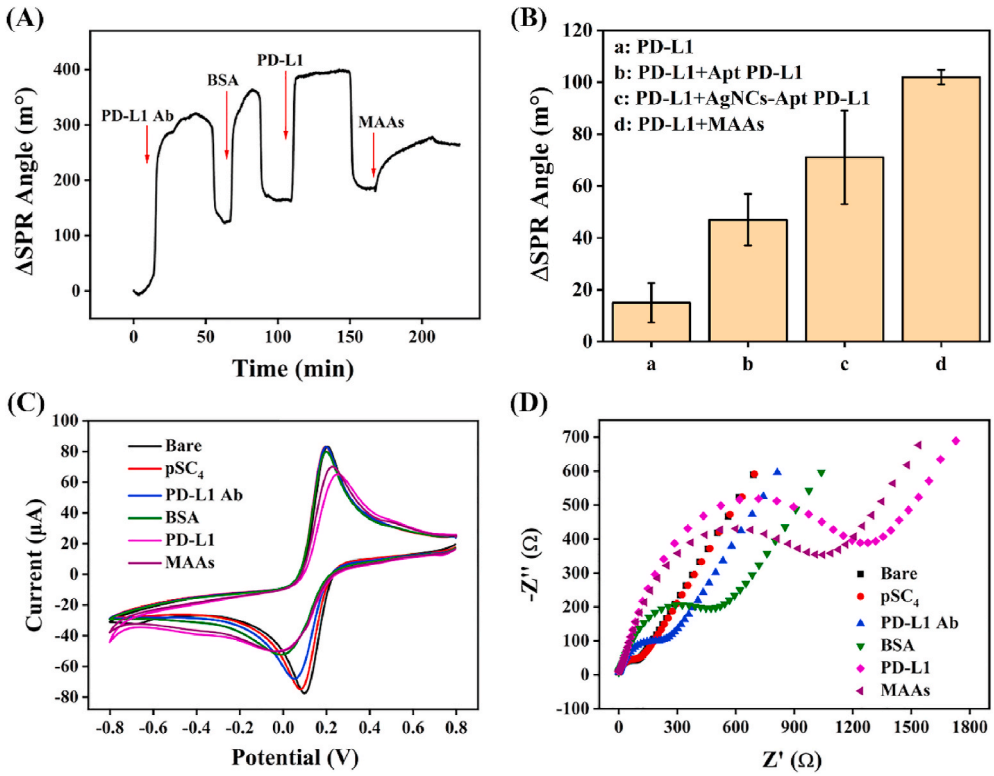

Fig. 3. Feasibility of the constructed biosensor for PD-L1 detection: (A) SPR angle shifts of different modified gold chips. (B) SPR angle change caused by PD-L1 only, PD-L1 and Apt PD-L1, PD-L1 and AgNCs-Apt PD-L1, and PD-L1 and MAAs. CV (C) and EIS (D) curves collected by each step of modification of the electrode in 5 mM $[Fe(CN)_6]^{3-/4-}$ containing 0.1 M KCl. (For interpretation of the references to color in this figure legend, the reader is referred to the Web version of this article.)

hydrophobic ligand determines poor biocompatibility and lack of functional groups on the surface of MNOM, which seriously hinders its application. Therefore, it is necessary to find a facile and effective method to achieve ligand exchange and surface functionalization of MNOM. Inspired by the thiol ligand exchange on the surface of FePt bimetallic nanoparticles (Bagaria et al., 2006), MUA is utilized to conduct oleylamine ligands exchange of MNOM and simultaneously functionalize the surface with thiol groups.

The FT-IR spectra of the MUA ligand and the as-made MNOM were shown in Fig. 1(A). The presence of –OH stretching vibrations at 3437 cm^{-1} of MNOM-MUA indicated the dispersed phase changes of the nanomaterials. The peak at 1585 cm^{-1} of –NH bending vibrations was disappeared due to the successful removal of oleylamine (Zhang et al., 2019). To further confirm the ligand exchange, MNOM with the OA and MUA ligand were added into 100 μL of deionized water (Fig. 1(A) inset) (Higbee-Dempsey et al., 2020). MNOM-MUA became soluble in water after ligand exchange while MNOM-OA was obvious immiscible owing to its hydrophobicity.

AFM was used to characterize the topography and surface roughness of MNOM-MUA, and the obtained images showed extremely low surface roughness in Fig. 1(B), which verified the nanorod structure of MNOM. The 3D image was shown in Fig. S1(A). The TEM images of Fig. 1(C) exhibted the uniform rod morphologies of MNOM-MUA with an average length of 50 ± 5 nm and an average width of 15 ± 2 nm. Fig. 1(D) and (E) were the high-resolution TEM (HRTEM) images of MNOM. The radius of the mesocages was about 3 nm as shown in Fig. 1(D). The SEM image (Fig. S1(B)) showed that MNOM-MUA were uniform nanorods, which was consistent with TEM.

Silver nanoclusters (AgNCs) are capable of binding onto MNOM by the affinity with thiol groups to fabricate magneto-optical nanocomplex and further enhance the optical properties of MNOM. TEM image in Fig. 1(F) and HRTEM images in Fig. 1(G) showed the good uniformity and dispersibility of AgNCs and the average size of AgNCs was around 3.62 nm. As depicted in Fig. S2, the energy dispersive spectra (EDS) results showed that the AgNCs were successfully synthesized and the surface plasmon resonance band of AgNCs was observed at 392 nm as Fig. S3.

With the aim of examining the successful functionalization of AgNCs onto MNOM-MUA, AFM, TEM-EDS and SEM-EDS were used. As seen from Fig. 2(A), after coupling AgNCs, the surface roughness was increased to about 4 nm when compared with Fig. 1(B) of MNOM-MUA, while the surface height was corresponded to the size of AgNCs. The 3D image was shown in Fig. S4(A). TEM image of MNOM@AgNCs was shown in Fig. 2(B) and the corresponding line scans were employed to investigate the element distributions as Fig. 2(C). The appearance of Ag element after magnetic separation confirmed the successful combination of AgNCs. The results in Figs. S4(B) and S4(C) were consistent with this result. In addition, the distribution tendency of intensity of Ag element was same as that of O and Fe elements, that is, the element intensity of three elements is relatively high in the range of 10 nm to 30 nm, which corresponds to the width of the MNOM. Furthermore, Fig. 2(D) exhibited the element mapping images recorded in the selected area, which indicated that O, Fe and Ag elements were uniformly distributed and the co-localization of these three elements confirmed the successful combination of AgNCs onto MNOM through EDS. The Zeta potential of AgNCs, MNOM-MUA and MNOM@AgNCs were shown in Fig. S4(D). These results all demonstrated the successful fabrication of MNOM@AgNCs.

3.2. Feasibility of the biosensor

SPR could be used to monitor stepwise modification process in real time. In order to verify the feasibility of the constructed sensor for detecting PD-L1, the process of the sensor was investigated by MP-SPR as shown in the Fig. 3(A). After modifying pSC4 onto the chip surface via Au–S bond, PD-L1 Ab could interact with the cavity of pSC4 through

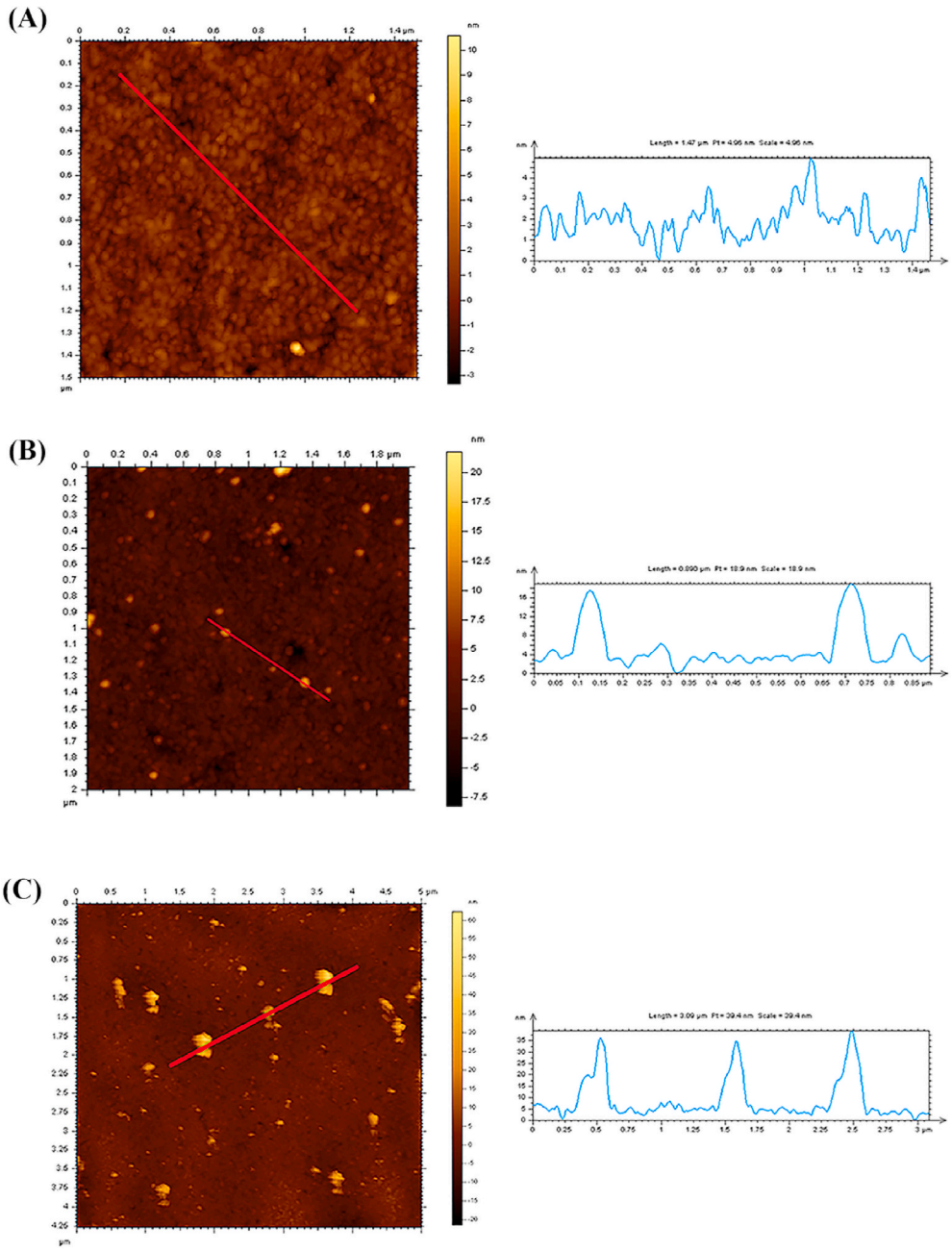

Fig. 4. Surface geometry of the constructed immunosensor: 2D AFM images (Left) and line profiles (Right) of bare gold chip (A), PD-L1 Ab/PD-L1 (B) and PD-L1 Ab/PD-L1/MAAs (C). (For interpretation of the references to color in this figure legend, the reader is referred to the Web version of this article.)

host-guest recognition and hydrophobic interaction, which resulted in a significant SPR angle shift. The SPR angle after modification of PD-L1 changed 15 m°. Through specific interaction of Apt PD-L1 and PD-L1, MAAs resulted 87 m° SPR angle shift. As shown in Fig. 3(B), the SPR angle shifts caused by PD-L1 and MAAs were almost 3 times and 1.5 times than that of Apt PD-L1 only and AgNCs-Apt PD-L1, respectively, which indicated the successful signal amplification of MAAs.

Electrochemical measurement methods included EIS and CV were utilized to further prove the feasibility of the sensor as Fig. 3(C) and (D). After each step of modification, the increasing diameter of the semicircle of EIS corresponded to the decrement of the redox peak in the CV, which implied that the modification of protein included PD-L1, BSA and PD-L1 Ab hindered the transfer of electron and was in line with expectations. Due to good conductivity of MNOM and AgNCs on MAAs, the impedance on the surface of the electrode was decreased and oxidation peak current was increased, confirming the feasibility of the developed sensor.

Atomic force microscope(AFM) analysis was utilized to observe the surface geometry of the constructed immunosensor at different fabrication stages on the gold chip. Fig. 4(A) showed the two-dimensional image and a typical cross-sectional line drawing of bare gold chip, and exhibited slight change of surface roughness. As depicted in Fig. 4(B), after modifying PD-L1 Ab and PD-L1, the height significantly increased to around 17 nm, which was in accordance with the height of PD-L1 Ab and PD-L1. Higher roughness when incorporating MAAs was about 35 nm as shown in Fig. 4(C). In addition, the shoulder peak of Fig. 4(C) was in line with the height of Fig. 4(B), further suggested the successful anchor of MAAs complex on PD-L1 Ab and PD-L1. The 3D images of Fig. 4(A) to 4(C) were shown in Figs. S5(A)–S5(C), respectively.

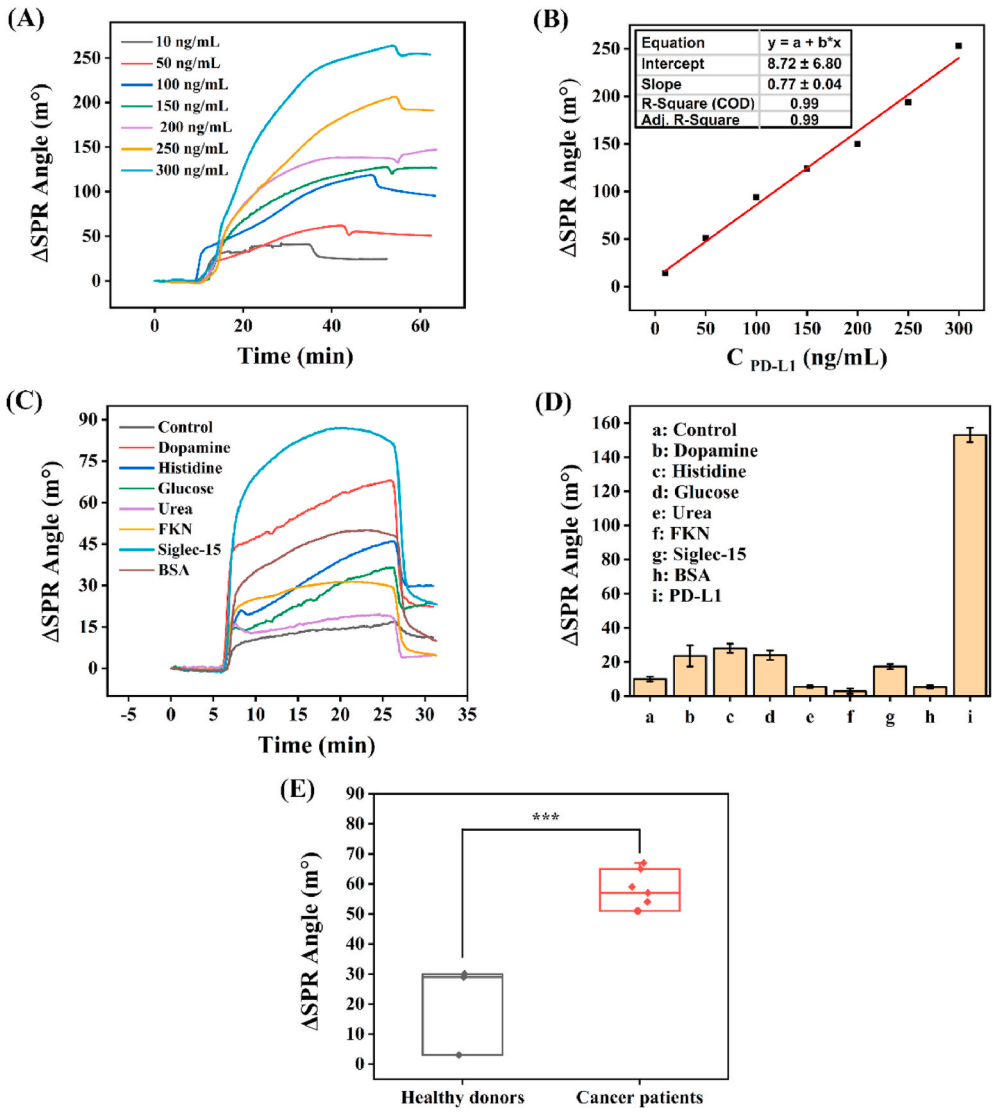

Fig. 5. Detection of PD-L1: The raw SPR sensorgram (A) and corresponding linear relationship (B) between different concentrations of PD-L1 and the SPR angle shifts caused by MAAs. (C) SPR angle shifts caused by different interference. (D) Comparison of the SPR angle shifts caused by target PD-L1 and interference. (E) SPR angle shifts caused by PD-L1 captured from healthy donors and cancer patients. Statistical comparison was performed with *t*-test (***$p < 0.001$).

3.3. Optimization of the experimental parameters

In order to obtain the best experimental results, four experimental conditions were optimized, including the concentration of pSC4, PD-L1 Ab and Apt PD-L1, and the volume ratio of MNOM to AgNCs. The same concentration of PD-L1 Ab was utilized to observe the SPR angle change caused by different concentrations of pSC4. As seen from Figs. S6(A) and 10 mM pSC4 caused the biggest SPR angle shift and was selected as the optimal concentration. In Fig. S6(B), SPR angle shift caused by 0.5 to 5 μg/mL PD-L1 Ab was investigated and it gradually increased along with the increment of the concentration, and almost saturated at 2.34 μg/mL, which was chosen as the best concentration for subsequent experiments. Apt PD-L1 was directly related to effect of signal amplification, and as depicted from Fig. S6(C), the SPR angle reached the maximum at 1 μM, which showed the best effect of signal amplification. The volume ratio of MNOM to AgNCs was shown in Fig. S6(D) and it turned out to be that 2:1 owned the most obvious SPR angle shift. The optimized conditions were utilized in further experiments.

3.4. PD-L1 detection by SPR

After optimizing the main parameters of the constructed sensor, the SPR angle shifts caused by different concentrations of PD-L1 (10 ng/mL to 300 ng/mL) were measured to verify the performance. As the concentration of PD-L1 varies greatly in different stages of cancer and the highest concentration of PD-L1 in cancer patients may reach 25 ng/mL, a wide range of PD-L1 detection is needed to meet the needs of clinical testing (Han et al., 2021; Wang et al., 2015; Zhu and Lang, 2017). As shown in Fig. 5(A) and (B), the biosensor exhibited a good linear relationship between the concentration of PD-L1 and the change in the SPR angle, and the linear equation was $y = 0.77x+8.72$ ($R^2 = 0.99$). The detection limit was calculated to be 3.29 ng/mL according to signal-to-noise ratio of 3. The enhanced electric field at the hotspots in the gap between MNOM@AgNCs magneto-optical nanocomplex and localized surface plasmon bands of AgNCs made the biosensor more sensitive to the changes in refractive index, which achieved a good improvement in performance. Table S1 showed the comparison between this work with other previous work. Although the detection limit was slightly higher than others, this strategy owned shorter reaction time and wider linear detection range, which can better meet the clinical

requirements of point-of-care testing.

Selectivity experiments were tested in the presence of possible interference, which included buffer (control), some small molecules and proteins in Fig. 5(C). Furthermore, the concentration of the interference is ten times higher than PD-L1. Serum biomarker fractalkine (FKN) mediated cell-cell adhesion and communication and played an indispensable role in Alzheimer's disease (Dong et al., 2018). Sialic acid binding immunoglobulin like lectins-15 (Siglec-15) as an immune suppressive molecule could be upregulated in many human cancers and its expression is mutually exclusive to PD-L1 (Wang et al., 2019). Thus, FKN and Siglec-15 were selected to evaluate the sensor's selectivity. As shown in Fig. 5(D), all the interference and the control group only showed slight change in the SPR angle when compared to that of the target protein, which demonstrated the excellent selectivity of the biosensor due to the dual selective recognition.

3.5. Detection of PD-L1 in blood samples

Blood samples were drawn from healthy donors and cancer patients from Shanghai Tenth People's Hospital, and collected in ethylene diamine tetraacetic acid (EDTA)-coated tubes and used within 24 h. All experiments on clinical samples were approved by the Medical Research Ethics Committee, Shanghai Tenth People's Hospital, Shanghai, China. The blood samples were placed at room temperature for 2 h and then centrifuge at 1000 g for 20 min to obtain the supernatant of serum, and stored at -80°C (Li et al., 2019). The collected serum was diluted one hundred times with PBS in pH 7.4 to test the practical feasibility of the constructed sensor. As shown in Fig. 5(E), the changes in SPR angle caused by cancer patients samples were greater than those caused by healthy donors with a statistically significant difference ($p < 0.001$), thereby indicating that this biosensing platform has the potential to detect PD-L1 in clinical applications.

4. Conclusion

In summary, magnetoplasmonic nanomaterials MNOM@AgNCs based SPR sensor was fabricated to achieve ultra-sensitive and quantitative detection of PD-L1. MNOM@AgNCs was prepared by coupling MNOM with AgNCs through Ag–S bond. Owing to the large specific surface area of MNOM and localized surface plasmon resonance of AgNCs, MNOM@AgNCs with excellent magneto-optical properties can synergistically enhance the detection sensitivity. The sandwich structure consisting of PD-L1 Ab, PD-L1 and Apt PD-L1 achieved dual recognition of PD-L1, which ensured the outstanding specificity of this strategy. The SPR angle shift obtained by MAAs was about three times that of only Apt PD-L1, which demonstrated the great signal amplification performance of MAAs. The low detection limit and a short reaction time met the requirements of clinical point-of-care testing. In addition, real samples detection indicated the great practical detection ability of this biosensor. The proposed strategy provided a great opportunity for detecting PD-L1 in clinical diagnosis.

CRediT authorship contribution statement

Xing Huang: Conceptualization, Data curation, Formal analysis, Validation, Writing – original draft. **Zhao-huan Zhang:** Data curation, Formal analysis, Writing – original draft. **Jie Chen:** Data curation, Formal analysis. **Zhihui Mao:** Data curation, Writing – review & editing. **Han Zhu:** Formal analysis, Writing – original draft. **Yawen Liu:** Data curation, Writing – review & editing. **Zhongzheng Zhu:** Conceptualization, Writing – review & editing. **Hongxia Chen:** Project administration, Funding acquisition, Writing – review & editing.

Declaration of competing interest

The authors declare that they have no known competing financial interests or personal relationships that could have appeared to influence the work reported in this paper.

Acknowledgment

This work was supported by the National Natural Science Foundation of China (Grant No. 61875114and 62005156).

Appendix A. Supplementary data

Supplementary data to this article can be found online at https://doi.org/10.1016/j.bios.2021.113385.

References

Adhikari, M., Echeverria, E., Risica, G., Mcilroy, D.N., Vasquez, Y., 2020. ACS Omega 5, 22440–22448.
Bagaria, H.G., Ada, E.T., Shamsuzzoha, M., Nikles, D.E., Johnson, D.T., 2006. Langmuir 22, 7732–7737.
Cialla-May, D., Zheng, X.S., Weber, K., Popp, J., 2017. Chem. Soc. Rev. 46, 3945–3961.
Deng, Y., Wei, J., Sun, Z., Zhao, D., 2013. Chem. Soc. Rev. 42, 4054–4070.
Dong, H., Hu, X., Zhao, J., Li, H., Koh, K., Gao, L., Chen, H., 2018. Sens. Actuators, B 276, 150–157.
Ferhan, A.R., Jackman, J.A., Park, J.H., Cho, N.J., Kim, D.H., 2018. Adv. Drug Deliv. Rev. 125, 48–77.
Han, B., Dong, L., Zhou, J., Yang, Y., Guo, J., Xuan, Q., Gao, K., Xu, Z., Lei, W., Wang, J., Zhang, Q., 2021. Cancer Immunol. Immun 1–17.
Hasanzadeh, M., Shadjou, N., Miguel, D.L.G., 2017. TrAC Trends Anal. Chem. (Reference Ed.) 91, 67–76.
Higbee-Dempsey, E.M., Amirshaghaghi, A., Case, M.J., Bouché, M., Tsourkas, A., 2020. J. Am. Chem. Soc. 142, 7783–7794.
Jayanthi, V.S.P.K.S.A., Das, A.B., Saxena, U., 2017. Biosens. Bioelectron. 91, 15–23.
Jiang, X., Wang, J., Deng, X., Xiong, F., Ge, J., Xiang, B., Wu, X., Ma, J., Zhou, M., Li, X., 2019. Mol. Canc. 18, 1–17.
Jiang, Y., Shi, M., Liu, Y., Wan, S., Cui, C., Zhang, L., Tan, W., 2017. Angew. Chem. Int. Ed. 56, 11916–11920.
Kim, J.M., Chen, D.S., 2016. Ann. Oncol. 27, 1492–1504.
Lee, J., Lee, J., 2017. Chem. Commun. 53, 5814–5817.
Li, M., Ding, H., Lin, M., Yin, F., Fan, C., 2019. J. Am. Chem. Soc. 141, 18910–18915.
Lv, S., Sheng, J., Zhao, S., Liu, M., Chen, L., 2018. Biosens. Bioelectron. 117, 138–144.
Murphy, C.J., Gole, A.M., Hunyadi, S.E., Stone, J.W., Sisco, P.N., Alkilany, A., Kinard, B. E., Hankins, P., 2008. Chem. Commun. 544–557.
Naaz, S., Poddar, S., Bayen, S.P., Mondal, M.K., Roy, D., KrMondal, S., Chowdhury, P., Saha, S.K., 2018. Sens. Actuators, B 255, 332–340.
O'Malley, D.P., Yang, Y., Boisot, S., Sudarsanam, S., Wang, J.F., Chizhevsky, V., Zhao, G., Arain, S., Weiss, L.M., 2019. Mod. Pathol. 32, 929.
Pang, Y., Shi, J., Yang, X., Wang, C., Sun, Z., Xiao, R., 2020. Biosens. Bioelectron. 148, 111800.
Qiao, X., Su, B., Liu, C., Song, Q., Luo, D., Mo, G., Wang, T., 2018. Adv. Mater. 30, 1702275.
Reguera, J., Langer, J., de Aberasturi, D.J., Liz-Marzán, L.M., 2017. Chem. Soc. Rev. 46, 3866–3885.
Saito, R., Abe, H., Kunita, A., Yamashita, H., Seto, Y., Fukayama, M., 2017. Mod. Pathol. 30, 427–439.
Saleh, T.A., Al-Shalalfeh, M.M., Al-Saadi, A.A., 2016. Sci. Rep. 6, 32185.
Singh, S., Gill, A.A.S., Nlooto, M., Karpoormath, R., 2019. Biosens. Bioelectron. 137, 213–221.
Song, S., Hu, X., Li, H., Zhao, J., Koh, K., Chen, H., 2018. Sens. Actuators, B 274, 54–59.
Sound, T.M., Kerr, K.M., Mark, K., Mary-Beth, B., Borczuk, A.C., Johan, B., Lukas, B., Lucian, C., Gang, C., Teh-Ying, C., 2018. J. Thorac. Oncol. 13, 1302–1311.
Tufa, L.T., Gicha, B.B., Wu, H., Lee, J., 2020. Batteries & Supercaps.
Wang, J., Sun, J., Liu, L.N., Flies, D.B., Nie, X., Toki, M., Zhang, J., Song, C., Zarr, M., Zhou, X., 2019. Nat. Med. 25, 656–666.
Wang, L., Wang, H., Chen, H., Wang, W., Chen, X., Geng, Q., Xia, Z., Lu, Y., 2015. Oncotarget 6, 41228.
Wu, H., Lee, D., Tufa, L.T., Kim, J., Lee, J., 2019. Chem. Mater. 2263–2268.
Wu, Q., Sun, Y., Zhang, D., Li, S., Wang, X., Song, D., 2016. Biosens. Bioelectron. 86, 95–101.
Ye, H., Yang, K., Tao, J., Liu, Y., Zhang, Q., Habibi, S., Nie, Z., Xia, X., 2017. ACS Nano 11, 2052–2059.
Yu, J., Xin, W., Teng, F., Li, K., 2016. OncoTargets Ther. 9, 5023–5039.
Zhang, J., He, M., Nie, C., He, M., Chu, X., 2019. Anal. Chem. 91.
Zhang, N., Liu, Y.J., Yang, J., Su, X., Deng, J., Chum, C.C., Hong, M., Teng, J., 2014. Nanoscale 6, 1416–1422.
Zhang, S., Li, H., Wang, Z., Liu, J., Zhang, H., Wang, B., Yang, Z., 2015. Nanoscale 7, 8495–8502.
Zhao, J., Liang, D., Gao, S., Hu, X., Koh, K., Chen, H., 2019. Biosens. Bioelectron. 141, 111440-111440.
Zhou, H., Zou, F., Koh, K., Lee, J., 2014. J. Biomed. Nanotechnol vol. 10, 2921–2949.

Zhu, J., Zhu, Y., Zhu, L., Rigutto, M., van der Made, A., Yang, C., Pan, S., Wang, L., Zhu, L., Jin, Y., 2014. J. Am. Chem. Soc. 136, 2503–2510.
Zhu, X., Lang, J., 2017. Oncotarget 8, 97671–97682.
Zhu, Z., Li, H., Xiang, Y., Koh, K., Chen, H., 2020. Microchim. Acta 187.